



A new non-equiautomic Ti40Zr25Nb25Ta5Al5 refractory high entropy alloy for potential biomedical applications

L. Mustafi ^a, V.T. Nguyen ^b, T. Song ^a, X.-B. Chen ^c, D.M. Fabijanic ^d, M. Qian ^{a,*}

^a Centre for Additive Manufacturing, School of Engineering, RMIT University, Melbourne, VIC 3000, Australia

^b School of Mechanical and Mining Engineering, The University of Queensland, Brisbane, Queensland 4072, Australia

^c School of Engineering, RMIT University, Melbourne, VIC 3000, Australia

^d Institute for Frontier Materials, Deakin University, Waurn Ponds, VIC 3216, Australia



ARTICLE INFO

Keywords:

High entropy alloy
Tensile
Mechanical
Deformation
Corrosion resistance

ABSTRACT

A non-equiautomic Ti40Zr25Nb25Ta5Al5 refractory high entropy alloy (RHEA) was designed for potential biomedical applications by replacing 5 at.% Ta with 5 at.% Al in a precursor Ti40Zr25Nb25Ta10 alloy. This simple and low-cost strategy reduced the alloy density from 7.2 to 6.5 g/cm³ (estimated using the 'rule of mixtures') and increased the yield strength (σ_{ys}) from 875 to 960 MPa, while still allowing the RHEA to achieve a high tensile ductility of about 17 % in the as-cast condition. Few bio-applicable metallic alloys can achieve such tensile strength-ductility combinations in the as-cast condition. Compared to the mill-annealed medical-grade Ti-6Al-4V (wt.%) alloy, this as-cast RHEA offers significantly higher yield strength and ductility, along with a much lower cytotoxic aluminium content (1.8 wt.%). Furthermore, the as-cast RHEA has a much higher admissible strain (1.12 %) than Ti-6Al-4V (0.75 %) and also exhibits better corrosion resistance in Hank's solution than Ti-6Al-4V. These evaluation results demonstrate the potential of this Ti40Zr25Nb25Ta5Al5 RHEA for biomedical applications. To elucidate the origin of these attractive properties, the solidification microstructure, tensile deformation mechanisms and surface oxide film of this RHEA were systematically investigated. A series of novel experimental observations were obtained and are discussed in detail.

1. Introduction

Refractory high entropy alloys/medium entropy alloys (RHEAs/RMEAs) are composed of high-melting-point metals, including Hf, Ta, Nb, Zr, Ti, Mo, W, V and Cr [1]. They offer attractive properties, including ultrahigh strength at room temperature (RT) [2–7] and excellent corrosion resistance [8–11]. Among the aforementioned elements, Ta, Nb, Zr and Ti are premier biocompatible metals, while Hf [12] and Mo [13] also have acceptable biocompatibility up to certain concentrations. Accordingly, RHEAs composed of some or all these six elements continue to attract widespread research interest as potential biomedical alloys.

Aluminium (Al) is not considered biocompatible and has been associated with serious conditions such as osteomalacia, Alzheimer's disease, and peripheral neuropathy [14]. Nonetheless, the titanium alloy Ti-6Al-4V containing 6 wt.% Al (~10 at.%) has been used as a primary implant alloy for decades, despite the known cytotoxicity of both Al and V [15,16]. Its widespread use for orthopedic applications is

expected to continue, perhaps forever. Interestingly, Al can effectively stabilize the body centred-cubic (BCC) structure (the phase of choice for RHEAs) and offers strong solid solution strengthening [17–20]. Therefore, Al has been introduced to a large number of promising bio-RHEAs for lower densities and higher strength, such as Al_{0.4}Hf_{0.6}NbTaTiZr [17, 18], AlMo_{0.5}NbTa_{0.5}TiZr [17,18,21], AlNb_{1.5}Ta_{0.5}Ti_{1.5}Zr_{0.5} [17], Al_{0.3}NbTaTi_{1.4}Zr_{1.3} [17], AlNbTa_{0.5}TiZr_{0.5} [21], AlMo_{0.5}NbTa_{0.5}TiZr_{0.5} [21,22], Al_{0.5}Mo_{0.5}NbTa_{0.5}TiZr [21], and Al_{0.25}NbTaTiZr [21]. Indeed, the density was reduced, and the strength was increased. However, this aluminium modification strategy resulted in significantly lower ductility, even under compression conditions [19]. Moreover, the modulus of elasticity (E) remained high (133 GPa [21]), which is a concern because of the possible 'stress shielding' effect between the implants and adjacent bones [23].

We have recently developed a strong and ductile (tensile) non-equiautomic bio-RHEA, Ti40Zr25Nb25Ta10, by replacing 15 at.% Ta in the equiautomic TiNbZrTa RHEA with 10 at.% Ti to ease lattice distortion [24,25]. This replacement not only reduces the density from 9 to

* Corresponding author.

E-mail address: ma.qian@rmit.edu.au (M. Qian).

7.2 g/cm³, but also remarkably increases the tensile ductility from 1 % to 18 %, while maintaining a high tensile yield strength (875 MPa) [24, 25]. This strong and ductile (tensile) non-equiautomic Ti40Zr25Nb25Ta10 RHEA serves as a unique precursor alloy for exploring the aluminum modification strategy in RHEAs.

Our strategy in this study involves replacing 5 at.% Ta in the Ti40Zr25Nb25Ta10 RHEA with 5 at.% Al. The goals of this substitution are to further reduce the high melting point, density, and material costs of the precursor Ti40Zr25Nb25Ta10 RHEA, while maintaining its excellent strength-ductility combination and ensuring acceptable biocompatibility. Thermodynamic simulations suggest that incorporating 5 at.% Al is unlikely to result in the formation of any brittle intermetallic phases. Additionally, the addition of 5 at.% Al (1.8 wt.%) is well below the 6 wt.% Al content found in the widely used medical-grade Ti-6Al-4V alloy, indicating acceptable biocompatibility (as discussed earlier, Al could raise serious concerns [26]). For these reasons, this study focuses on the Ti40Zr25Nb25Ta5Al5 RHEA. Previous studies focusing on adjustments to the Ti and Ta content [24,25] have proven highly effective. If this new strategy proves successful, it will enhance the appeal of this RHEA due to its resulting lower melting point, density, and material costs.

2. Materials and methods

2.1. Sample preparation

Ti40Zr25Nb25Ta5Al5 (at.%) RHEA was fabricated from elemental nuggets with a minimum purity of 99.95 wt.% using an arc melting furnace (AM200, Edmund Bühler GmbH) under a Ti- getter pure Ar-atmosphere. Firstly, five alloy buttons (~20 g) were fabricated. Each alloy button underwent six rounds of remelting to ensure chemical homogeneity, with each button flipped before each remelting cycle. Throughout each melting cycle, the alloy was kept in the liquid state for 10 min. Subsequently, all five buttons were combined and remelted together before being cast into a water-cooled Cu-mould to form a cuboidal bar with dimensions of 90 × 12 × 8 (thickness) mm³. Cross-sections of the as-cast alloy bar were ground using SiC abrasive papers and mirror-polished using 0.04 µm colloidal silica suspension (OPS) with 30 % H₂O₂ (10:1 by volume) for microstructural characterization.

2.2. Phase and microstructure characterization

The phase stability of the Ti40Zr25Nb25Ta5Al5 RHEA was predicted using the Pandat™ software and the PanNb2019 database, both developed by CompuTherm based on the CALPHAD approach. The phase formation of the Ti40Zr25Nb25Ta5Al5 RHEA was also predicted using the Empirical Rules [27]. The atomic mismatch δ (%), mixing enthalpy ΔH_{mix} (kJ/mol), mixing entropy ΔS_{mix} (J/mol K), and valence electron concentration (VEC) were the main design parameters used to calculate the phase formation in the alloy, and the calculations are detailed in [27–29]. Our designed Ti40Zr25Nb25Ta5Al5 RHEA corresponds to $\delta = 4.6\%$, $\Delta H_{mix} = -3.78\text{ kJ}\cdot\text{mol}^{-1}$, $\Delta S_{mix} = 11.3\text{ J}\cdot\text{mol}^{-1}\text{ K}$ and VEC = 4.2, which predicts BCC phase formation in this alloy [30,31].

Phase identification was performed using X-ray diffraction (XRD) (Bruker D8 Advance MKII with a monochromatic of Cu K α radiation) at the wavelength of Cu K α = 1.54056 Å, operated at 40 kV with a step size of 0.02°. Microstructure was analysed using scanning electron microscopy (SEM, JEOL, JSM-7200F, Japan), equipped with an energy dispersive spectrometry (EDS) detector (Oxford XMax20) and an electron backscattered diffraction (EBSD) detector (Oxford Instruments, NordlysMax2). The BCC structure was adopted for phase identification during EBSD characterisation and the lattice parameter 3.33 Å (calculated from XRD spectra) was utilized for collecting the EBSD data. Samples were tilted to an angle of 70° and all EBSD analyses were performed using an accelerating voltage of 15 kV, a probe current of 13 nA, and a step size of 1.5 µm. The EBSD results were analysed using

HKL's CHANNEL5 software.

Transmission electron microscopy (TEM) and high-resolution TEM (HRTEM) were conducted using a TEM instrument (JEOL 2100F, JEOL, Japan) operated at 200 keV in bright-field (BF) and selected area electron diffraction (SAED) modes. Scanning transmission electron microscopy (STEM) combined with EDS was used to characterize solidification grain boundaries (GBs). TEM samples were prepared using the standard lift-out method in a focused ion beam (FIB) system with FEI Scios DualBeam (FEI Scios DualBeam, Thermo Fisher Scientific, USA). A protective platinum (Pt) layer was deposited on sample surface prior to milling to minimize FIB-induced damage.

2.3. X-ray photoelectron spectroscopy (XPS) analysis

Analysis of surface chemistry was performed using a Kratos AXIS Supra XPS system (Kratos, Manchester, UK) equipped with dual monochromated X-ray sources (Al K α , Ephoto = 1486.7 eV). Prior to XPS characterization, samples were stored in lab environment (23 °C; humidity: 35–40 %) for 48 h to passivate the oxide films in the air. After that, it was transferred to a vacuum desiccator for 24 h to remove residual surface-absorbed water and minimise further surface contamination. XPS spectra were obtained at take-off angles of 0° with respect to the analyser. Quantification was achieved by fitting data in CasaXPS, using Shirley-type background models and Gaussian-Lorentzian product peaks [32].

2.4. Tensile testing

Dog-bone-shaped tensile samples with gauge dimensions of 8 mm × 2.9 mm × 1.5 mm (thickness) (Australian Standard AS 1391–2007) were prepared from as-cast bars using an electrical discharge wire-cutting machine. The entire surface of each tensile sample was ground with 600 grit SiC papers to remove the heat-affected layers from wire cutting. Tensile testing was performed on an Instron 5584 EM frame machine with a video extensometer. HEAs do not always show clear tensile yielding due to limited tensile ductility. In that scenario, their proof strength can be used as an estimate of yield strength. All tensile samples were tested at a slow strain rate of $5 \times 10^{-5}\text{ s}^{-1}$ at room temperature. The slow strain rate was selected by considering both ISO 6892-1 (Range 1 strain rate for the determination of proof strength: $7 \times 10^{-5}\text{ s}^{-1} \pm 20\%$) and ASTM E8/E8M – 15a (strain rate in the range of $5 \times 10^{-5}\text{ s}^{-1}$ to $1.2 \times 10^{-4}\text{ s}^{-1}$ for the determination of yield strength by aerospace specifications).

2.5. Density calculation

The density of the Ti40Zr25Nb25Ta5Al5 RHEA was estimated using the 'rule of mixtures', similar to the density estimation approach commonly used for other HEAs [1,7]:

$$\rho = \frac{\sum c_i A_i}{\sum \frac{c_i A_i}{\rho_i}}$$

where c_i , A_i , and ρ_i are the concentration, atomic weight and density of the element i , respectively.

2.6. Electrochemical characterization

Electrochemical characterization of the as-cast Ti40Zr25Nb25-Ta5Al5 RHEA and mill-annealed ELI Ti6Al4V alloy was performed using a VMP 300 potentiostat, coupled with a three-electrode flat cell setup using a 2.5 cm × 2.5 cm platinum mesh as counter electrode and Ag/AgCl (+0.197 V_{SHE}) as reference electrode. Standard Hank's solution was used as electrolyte [33]. The pH value was adjusted to 7.2–7.6 with 1 M HCl. In thermostatic incubator 5 % CO₂ was used to replicate physiological conditions and the temperature of the incubator was

maintained at 37 °C [34–36]. The working electrodes were specimens connected with a conductive copper wire extension embedded in epoxy. A constant cross-section of 0.1 cm² was exposed to Hank's solution. Prior to testing, epoxy-mounted specimens were polished progressively up to 1200 grit SiC paper, degreased with acetone and ethanol, rinsed with distilled water, and dried in a compressed air stream. A desiccator was used for sample storage and transfer purposes. After 2 h immersion in Hank's solution to attain an electrochemically quasi-stable state, potentiodynamic polarisation plots were recorded in the range –0.2 to 2.5 V in relation to open circuit potential at a scan rate of 4 mV/s. To ensure consistency, each electrochemical measurement was repeated three times. Electrochemical data were collected on EC-lab software (V11.42).

3. Results and discussion

3.1. Phase prediction and identification by XRD

The solidification process of the Ti40Zr25Nb25Ta5Al5 RHEA is predicted in Fig. 1a using the Pandat™ simulation software. The simulation predicted a single BCC phase after solidification, in line with the calculations from the Empirical Rules of HEAs. The predicted solidification gap is 145 °C, compared to 311 °C for the precursor Ti40Zr25Nb25Ta10 RHEA. The solidus temperature of this alloy is 1730 °C, below which a BCC#1 phase was predicted until reaching 460 °C. In addition, a BCC#2 phase was predicted to form below 710 °C, which co-exists with a hexagonal close-packed (HCP) phase below 470 °C and an intermetallic phase (AlZr₂) below 450 °C.

The XRD pattern obtained from the copper mould-cast Ti40Zr25Nb25Ta5Al5 RHEA is shown in Fig. 1b. Only a BCC phase was detected, with the lattice parameter (*a*) of 3.28 Å, close to the lattice parameter of 3.35 Å estimated using Vegard's law [37]. The HCP and AlZr₂ phases, predicted to form below 470 °C and 450 °C, respectively, were not detected in XRD analysis. Subsequent TEM characterization also failed to identify the presence of either phase. This discrepancy can be attributed to the high cooling rates during copper-mould casting, which significantly deviate from the equilibrium cooling conditions assumed in the thermodynamic predictions using Pandat™. The rapid copper-mould cooling process results in a higher concentration of each element being retained within the BCC phase, hindering the precipitation kinetics of both the HCP and AlZr₂ phases and thereby suppressing their formation. However, based on computational thermodynamic predictions, long-term isothermal annealing below 450 °C is expected to

facilitate the formation of both phases.

3.2. Microstructure characterization

Fig. 2a-b shows the inverse pole figure (IPF) and the phase map of the as-cast Ti40Zr25Nb25Ta5Al5 RHEA. The grain structure is nearly equiaxed but contains some elongated or irregularly shaped grains, Fig. 2a. Some dendrites exhibit dimensions larger than the grain size. Similar observations have been reported in other BCC HEAs [1,38], where the decoupling of grain boundaries from dendrite boundaries was noted. This phenomenon represents an atypical solidification behaviour in concentrated alloys. The uneven contrast in many grains indicates the presence of sub-grains or low-angle grain boundaries (LAGBs). The average grain size was 131 ± 80 µm, much finer than the average grain size for the as-cast precursor Ti40Zr25Nb25Ta10 RHEA (250 µm [24]). This significant grain refinement resulting from the addition of Al is similar to that observed in the HfNbTaTiZr HEA following the introduction of Al [19]. The EBSD phase map (Fig. 2b) shows the existence of a single phase, in line with the XRD results in Fig. 1b.

SEM-BSE observations of the as-cast Ti40Zr25Nb25Ta5Al5 RHEA revealed a highly dendritic internal structure within each equiaxed grain, Fig. 3a. The compositional variations between the dendrites and inter-dendritic regions are due to micro-segregation during the solidification process, Fig. 3b. The dendrite arms are enriched in Ta and Nb (higher melting point elements), while the inter-dendritic regions are enriched in Ti, Zr and Al (lower melting point elements). This suggests that the solidification process still follows $k < 1$ (k : solute distribution coefficient) after introducing Al. Detailed results are summarised in Table 1.

Solidification grain boundaries (SGBs) result from the solidification of the last liquid between two adjacent grains of different orientations [24,25,38–40]. This last liquid is expected to be enriched with lower melting-point elements, which refer to Ti, Zr and Al in this RHEA. Indeed, EDS line-scan analysis confirmed that the SGB region is highly enriched with Ti, Zr and Al, as shown in Fig. 3c-d.

It is worth noting that mixing enthalpy ΔH_{mix} (kJ·mol^{–1}) is one of the key parameters used to estimate the phase formation in a HEA based on the Empirical rules [27–29]. The ΔH_{mix} between Zr and Ti is 0 kJ·mol^{–1} (predicted using Miedema's model [41]), implying that Zr and Ti tend to reside together. Nb and Ta have the same tendency due to their zero-mixing enthalpy. In contrast, Zr has a high ΔH_{mix} with both Nb and Ta, which means that Zr prefers to separate from both Nb and Ta. Al-Zr and Al-Ti have more negative ΔH_{mix} values than Al-Nb and Al-Ta. In

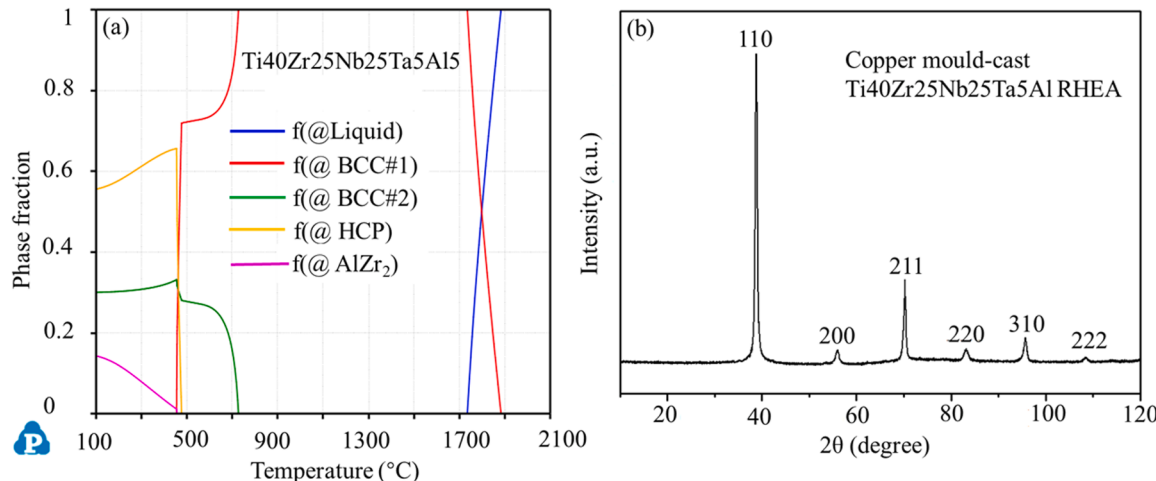


Fig. 1. (a) Phase prediction in the Ti40Zr25Nb25Ta5Al5 RHEA from the liquid state to 100 °C using the Pandat™ and Nb2019 database. (b) XRD pattern obtained from the copper mould-cast Ti40Zr25Nb25Ta5Al5 RHEA. BCC: body centred cubic. HCP: hexagonal close-packed. BCC#1 and BCC#2 refer to BCC phases with different compositions.

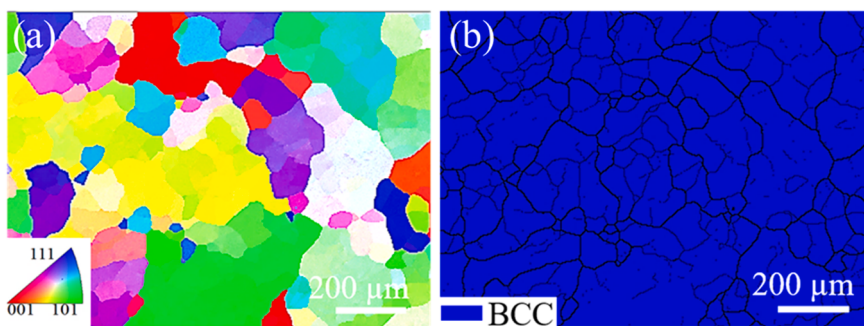


Fig. 2. EBSD characterization of the copper mould-cast Ti40Zr25Nb25Ta5Al5 RHEA: (a) an EBDS-IPF image (IPF: inverse pole figure) and (b) an EBSD phase map showing the existence of a single phase (BCC).

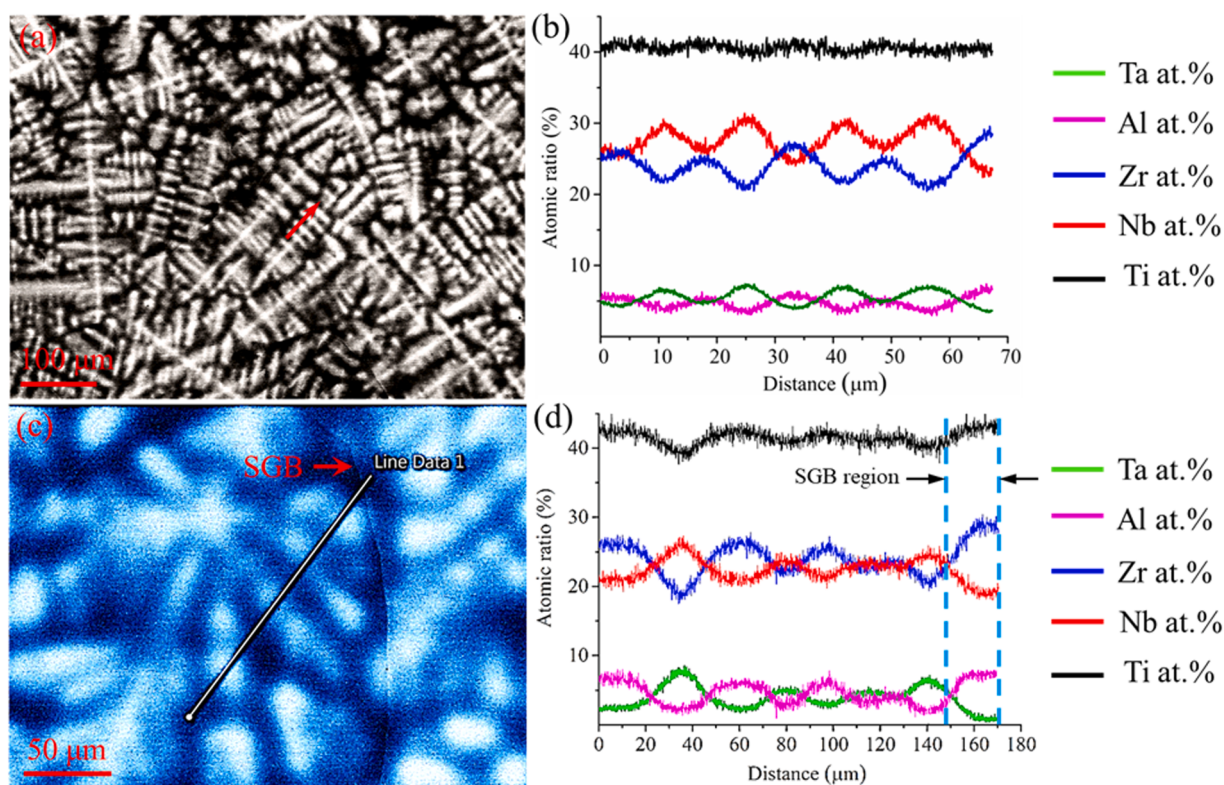


Fig. 3. (a) An SEM-BSE image of the as-cast Ti40Zr25Nb25Ta5Al5 RHEA and (b) EDS line-scan analysis across the red arrow line in (a) to investigate the micro-segregation of each element during solidification. (c, d) EDS line-scan analysis across both a dendrite and a solidification grain boundary (SGB) region in the as-cast Ti40Zr25Nb25Ta5Al5 RHEA, confirming that the SGB region is enriched with Ti, Zr and Al.

Table 1
Micro-segregation in the as-cast Ti40Zr25Nb25Ta5Al5 RHEA by SEM-EDS.

Region	Element (at.%)				
	Ti	Zr	Nb	Ta	Al
Inter-dendritic	42.6	27.9	21.5	2.7	6.1
	± 0.7	± 0.8	± 0.7	± 0.3	± 0.6
Dendrite	39.8	21.1	28.6	7.4	3.6
	± 0.9	± 0.9	± 0.9	± 0.4	± 0.9
Average	41.2	24.5	25.0	5.0	4.8
	± 0.9	± 0.7	± 0.5	± 0.8	± 0.9

other words, Al tends to choose Zr and Ti rather than Nb and Ta. The ΔH_{mix} values calculated using Miedema's model [41] for atomic pairs between constituent elements in the Ti40Zr25Nb25Ta5Al5 RHEA are listed in Table 2.

Table 2

Mixing enthalpy values (ΔH_{mix} , $\text{kJ}\cdot\text{mol}^{-1}$) calculated using Miedema's model [41] for atomic pairs between constituent elements in the Ti40Zr25Nb25Ta5Al5 RHEA.

Parameter	Elements	Ti	Zr	Nb	Ta	Al
Mixing enthalpy, ΔH_{mix} ($\text{kJ}\cdot\text{mol}^{-1}$)	Ti	–	0	2	1	–30
	Zr	–	–	4	3	–44
	Nb	–	–	–	0	–18
	Ta	–	–	–	–	–19
	Al	–	–	–	–	–

This ΔH_{mix} -based prediction coincides with the EDS results, where the dendrite is enriched with Nb and Ta, while the inter-dendritic areas are enriched with Ti, Zr and Al based on solidification predictions according to their melting points.

Pandat simulations predicted the formation of the AlZr_2 phase in this

RHEA (Fig. 1). Given the evident enrichment of Al and Zr in SGB regions, as depicted in Fig. 3c-d, further investigation was conducted by focusing on analysis of the SGB regions using HRTEM. Fig. 4a shows a representative HRTEM image taken from a selected SGB region in the as-cast Ti40Zr25Nb25Ta5Al5 RHEA. The inset is a selected area electron diffraction (SAED) pattern obtained after titling the darker grain to its [011] zone-axis. The diffraction spots confirmed the existence of only the BCC phase – a disordered solid solution phase. Fig. 4b is the STEM image of the same SGB region in Fig. 4a, while Fig. 4c shows the EDS line-scan analysis for each element across this region. No signs of Al₂Zr₂ and other secondary phases were observed. The absence of the Al₂Zr₂ phase can be attributed to the high cooling rates associated with the Cu-mould casting process, which restricted elemental segregation and shortened the reaction time between Al and Zr, thereby preventing the formation of formation of Al₂Zr₂.

3.3. Tensile properties

Fig. 5a shows the engineering tensile stress-strain curves obtained from the as-cast Ti40Zr25Nb25Ta5Al5 RHEA at RT. The alloy exhibited a strain to fracture of $16.6 \pm 2.2\%$, an ultimate tensile strength (σ_{UTS}) of 1020 ± 4.1 MPa and a tensile yield strength (σ_{ys}) of 959.4 ± 6.1 MPa. The tensile yield strength increased by about 10 % compared to that of the precursor Ti40Zr25Nb25Ta10 RHEA [24], due to the strong solid-solution strengthening effect of Al. These are outstanding tensile properties for as-cast RHEAs – strong and highly ductile. The tensile fracture surface shows clear dimpled fracture features, supporting the measured high tensile ductility, Fig. 5b-c. Table 3 compares the mechanical properties of this as-cast RHEA with other bio-RHEAs as well as biomedical Ti-6Al-4V and Ti-6Al-7Nb alloys.

The elastic modulus (E) of the as-cast Ti40Zr25Nb25Ta5Al5 RHEA was 85 ± 3.2 GPa versus 100 GPa for CP-Ti [54] and 120 GPa for Ti-6Al-4V [58]. Elastic admissible strain ($\psi = \sigma_{ys}/E$) is an important indicator for the selection of bone implant materials [59–64]. So, the higher the ψ , the more suitable the alloys for orthopaedic applications [61,62]. The ψ of the as-cast Ti40Zr25Nb25Ta5Al5 RHEA is 1.12 %, which is significantly higher than those for Ti-6Al-4V (0.75 %) and Ti-6Al-7Nb (0.65 %), both of which are important US-FDA-approved (United States Food and Drug Administration) orthopaedic titanium alloys. Fig. 6 compares the ψ values versus density for various

bio-RHEAs, Ti-6Al-4V and Ti-6Al-7Nb. The as-cast Ti40Zr25Nb25-Ta5Al5 RHEA shows a very high ψ value with a reasonable density (6.5 g/cm^3). It is noteworthy that the specific strength of this new RHEA Ti40Zr25Nb25Ta5Al5 ($148 \text{ MPa} \cdot \text{cm}^3/\text{g}$) is also higher than that of the precursor Ti40Zr25Nb25Ta10 RHEA ($115 \text{ MPa} \cdot \text{cm}^3/\text{g}$) [24].

3.4. Tensile deformation mechanisms

The fractured tensile specimens were polished to investigate the deformation mechanisms of this as-cast strong and ductile RHEA using SEM-BSE, EBSD and TEM. The analysis was focused on areas close to the fracture surface. Fine primary shear bands (band thickness $< 5 \mu\text{m}$) were prevalent after tensile deformation, Fig. 7a (SEM-BSE), and the length of these shear bands is constrained by the grain size or GBs. Furthermore, the formation of finer secondary shear bands within the primary shear band regions was also observed, Fig. 7b (BF-TEM image). These secondary shear bands are typically 100–500 nm wide. Their formation can be attributed to the strain localization during the significant plastic deformation process. The existence of primary and secondary shear bands within individual grains played a crucial role in enhancing the strength and ductility of this RHEA. Fig. 7c revealed the misorientation within deformed grains through the colour gradient, demonstrating non-uniform or inhomogeneous intragranular deformation. An EBSD band contrast image is shown in Fig. 7d, where traces of the primary shear bands (fine lamellae) are common.

No phase change was detected after the tensile deformation according to the EBSD phase map shown in Fig. 7e. The misorientation angles between the shear bands and the β matrix were measured to determine the types of deformation products. Fig. 7f shows the corresponding misorientation profiles of the deformation bands in Fig. 7c. Four misorientation profiles were determined, corresponding to the four directions of the arrows in Fig. 7c. The misorientation angles between the deformation products and the β -phase matrix were determined to be in the range of 2–20°, which confirmed that these misorientation profiles belong to the shear bands (rather than mechanical twins in BCC alloys that form 50.5° for {332} <113> or 60° for {112} <111> [65–67].

To gain further insight into the deformation mechanisms, post-mortem TEM characterization was conducted on the necking region after tensile fracture. Fig. 8a displays a TEM-BF image of a GB region near the fracture surface after 17 % tensile elongation, revealing a high density of dislocations within the GB region. SAED patterns, taken along the [012] zone-axis from the dark grain in Fig. 8a, confirm the exclusive presence of the BCC matrix phase. This indicates that no phase transformation or new phase formation occurred during the significant tensile deformation. Fig. 8b provides a magnified view of the dislocation distribution within the yellow-boxed area (b) in Fig. 8a. After this significant tensile elongation, the BCC matrix of this RHEA exhibited a significant density of dislocations in various configurations, including dislocation loop-like features. These diverse dislocation configurations are indicative of an active dislocation multiplication process during tensile deformation, which accounts for the high tensile ductility observed in this RHEA. Similar deformation behavior, characterized by the presence of various dislocation configurations including dislocation loops, has been reported in other ductile HEAs and RHEAs, such as the HfNbTiZr HEA, Ti40Zr25Nb25Ta10O0.5 HEA, and Ti1.5ZrNbAl0.3 RHEA [11,68,69].

Based on these observations, it can be concluded that the tensile deformation of the Ti40Zr25Nb25Ta5Al5 RHEA primarily occurs through the formation of both primary and secondary shear bands within individual grains, accompanied by the formation of dislocation loops. In contrast, after tensile deformation, the precursor Ti40Zr25Nb25Ta10 HEA is predominantly characterized by the presence of primary shear bands [24]. It should be emphasized that both the precursor Ti40Zr25Nb25Ta10 RHEA and the Ti40Zr25Nb25Ta5Al5 RHEA exhibit excellent combinations of tensile strength and ductility. However, the replacement of 5 at.% Ta with 5 at.% Al has resulted in the

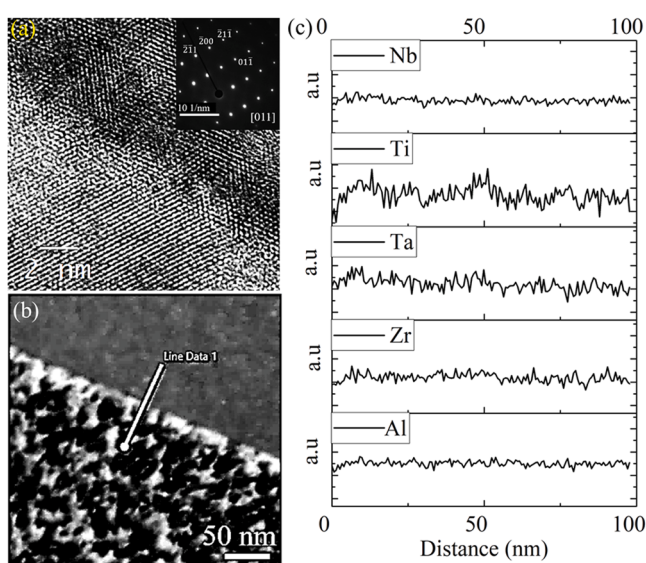


Fig. 4. TEM characterization of the as-cast Ti40Zr25Nb25Ta5Al5 RHEA: (a) HRTEM image of a SGB area, with the inset showing SAED pattern obtained after titling the darker grain to its [011] zone-axis; (b) STEM image of the SGB area in (a); and (c) EDS line-scan profiles of each element in (b).

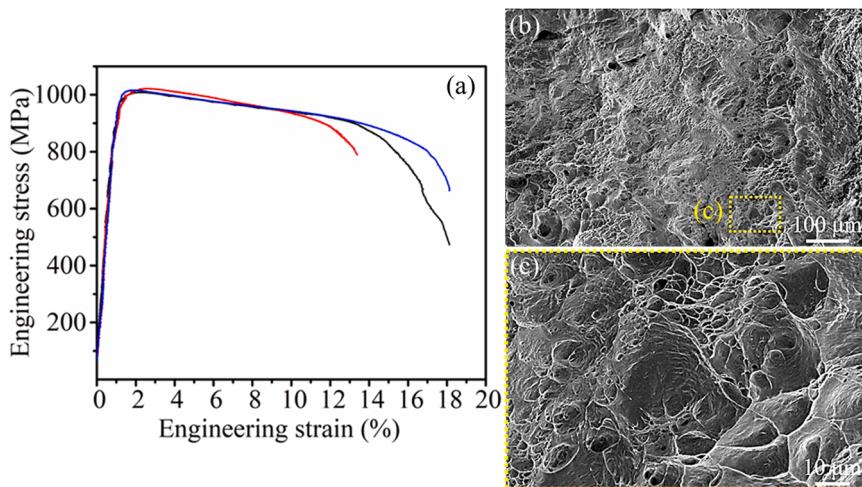


Fig. 5. (a) Engineering tensile stress-strain curves of the as-cast Ti40Zr25Nb25Ta5Al5 RHEA at RT; (b) SEM tensile fractograph of the RHEA; and (c) magnified view of the yellow rectangle (c) in (b).

Table 3

Tensile properties of as-cast Ti40Zr25Nb25Ta5Al5 RHEA and reported bio-applicable MEAs/HEAs as well as Ti-6Al-4V and Ti-6Al-7Nb alloys.

Alloys	σ_y (MPa)	σ_{UTS} (MPa)	ε_{Total} (%)	E (GPa)	ψ (%)	ρ (g/cm ³)	Ref.
Ti40Zr25Nb25Ta5Al5 RHEA	960	1020	~17	85	1.12	6.5	This study
Ti40Zr25Nb25Ta10 RHEA	875	925	18	77	1.13	7.6	[24]
Ti48.9Zr32 Nb12.6Ta6.5 MEA	643	694	23.8	64.6	0.99	6.5	[42]
NbTaTiZr HEA	1144	1205	6.4	98	1.16	~9	[43]
NbTaTi MEA	620	683	18.5	143	0.43	~10	[43]
TaTiZr MEA	—	284	0	157	0	~9	[43]
NbTiZr MEA	956	991	14.2	88	1.08	6.5	[43]
Nb1.5TaTiZr0.5 MEA	822	852	0.33	127	0.64	9.3	[43]
Nb0.5TaTiZr1.5 MEA	—	843	0	93	0	8.6	[43]
Ti30Zr38Nb20Ta8Sn4 HEA	1090	1190	24	77.7	1.4	7.24	[43]
Ti45Zr37Nb16Fe1Mo1 MEA	670	700	27	69	0.97	6.03	[44]
Ti35Zr15Nb25Ta25 MEA	842	873	17	91	0.93	8.8	[38]
Ti-6Al-4 V (wt.%)	898	981	3.0	120	0.74	4.4	[45]
Ti-6Al-4V ELI (wt.%) ^a	760-875	825-965	8-15	101-110	0.75	4.4	[46-54]
Ti-6Al-7Nb (wt.%)	824	1045	3.7	126	0.65	4.5	[55,56]
Ti-6Al-7 Nb (wt.%) ^a	800	900	10	-	-	4.5	[57]

^a Mill annealed. The remaining alloys are as-cast.

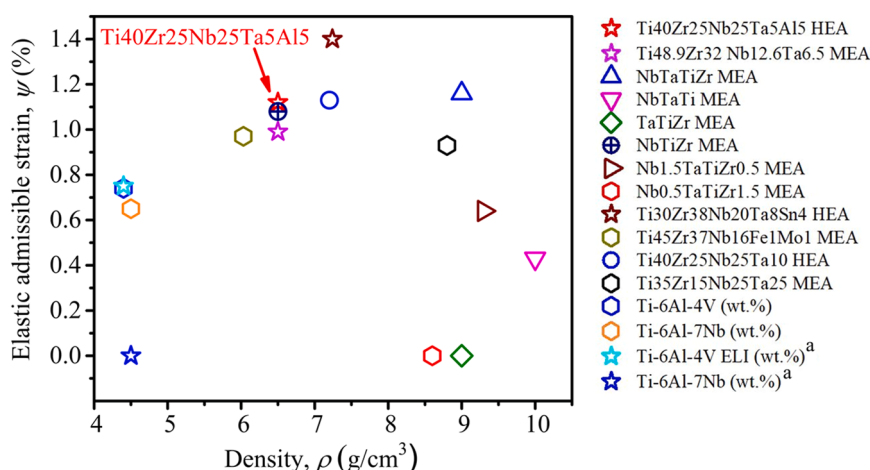


Fig. 6. Elastic admissible strain vs density for the as-cast Ti40Zr25Nb25Ta5Al5 RHEA and other bio-RHEAs as well as Ti-6Al-4V and Ti-6Al-7Nb (data source: Table 3).

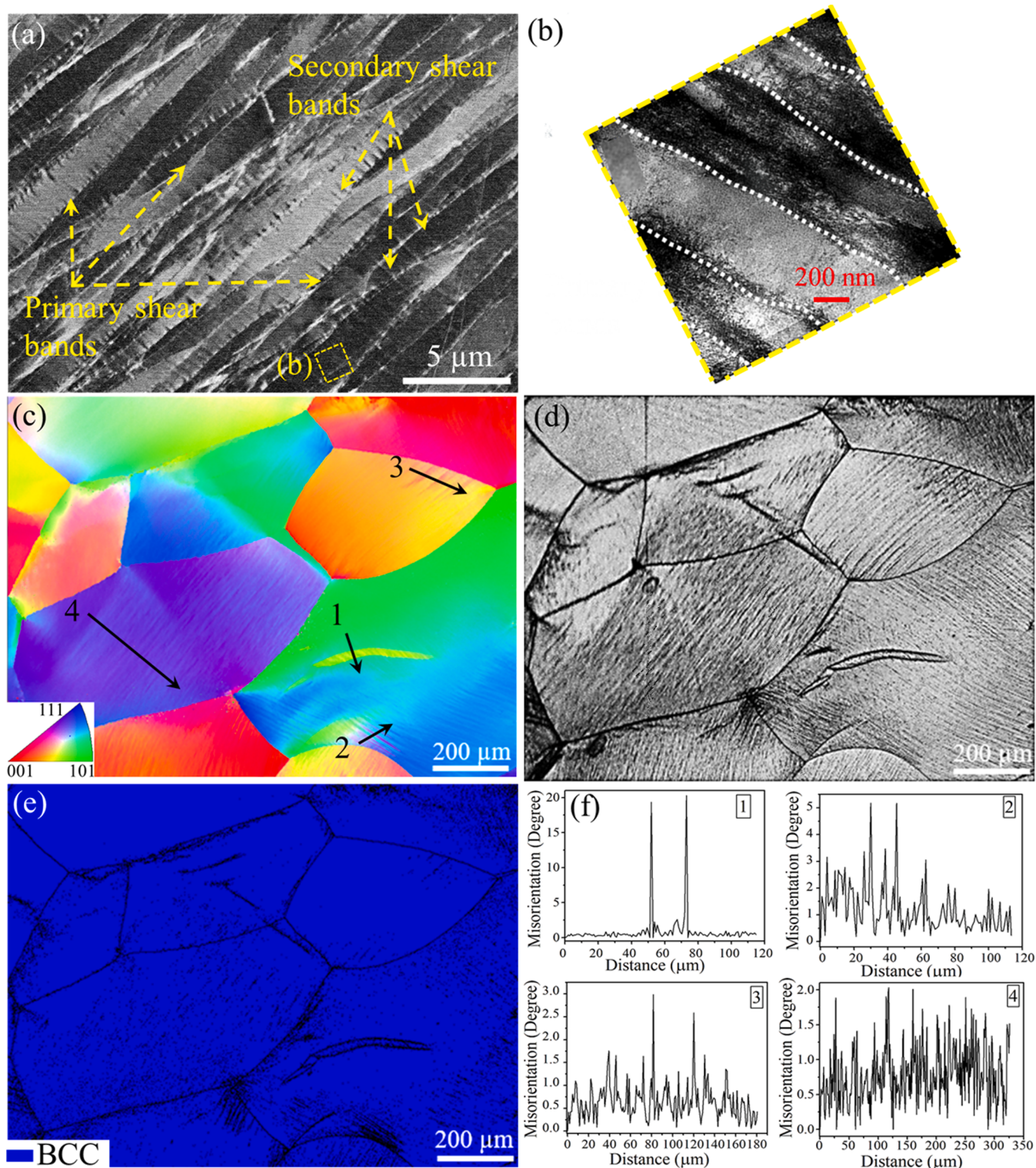


Fig. 7. Tensile deformation of the as-cast Ti40Zr25Nb25Ta5Al5 RHEA. (a) SEM-BSE image showing primary shear bands; (b) TEM-BF image revealing secondary shear bands taken from the yellow rectangle (b) in (a); (c) EBSD-IPF image after tensile testing; (d) EBSD band contrast map; (e) EBSD phase map showing a single phase (BCC); and (f) misorientation profiles between the primary bands and the β -matrix corresponding to the four arrows in (c).

following important changes:

- (i) Microstructural Refinement: The microstructure becomes much finer and more uniform, with the average grain size almost halved from 250 μm to 131 μm . This refinement supports the achievement of a high strength-ductility combination.

- (ii) Elemental Distribution: Al, which has the lowest melting point in this RHEA, is enriched in the interdendritic and SGB regions, while Ta, with the highest melting point, is primarily located in the dendrite trunk and arms, contributing to solid solution strengthening (Fig. 3). The replacement of 5 at.% Ta with 5 at.% Al reduces the Ta partition in dendrite trunks and arms,

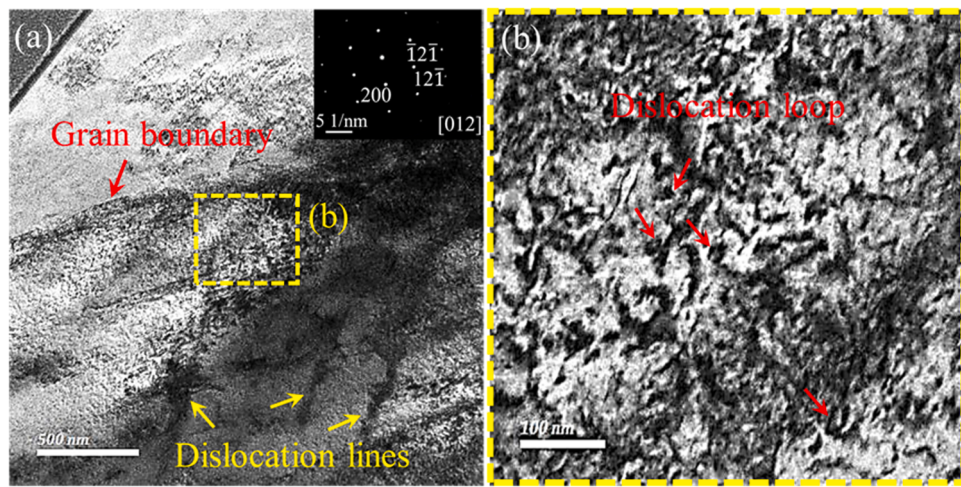


Fig. 8. TEM bright field (BF) characterization of the as-cast Ti40Zr25Nb25Ta5Al5 RHEA after tensile fracture. (a) A representative GB region near the tensile fracture surface with dislocation lines near the GB region, the inset is a SAED pattern of the dark grain obtained along the [012] zone axis; and (b) Dislocation loops near the GB region taken from the yellow rectangle (b) in (a).

alleviating the solid solution strengthening gradient caused by Ta within each grain. This allows for better coordination of deformation.

Nonetheless, given that the Al content is only 5 at.%, the fundamental characteristics of the precursor alloy remain largely unchanged. The advantages of this substitution are evident: reduced density, lower material costs, and enhanced manufacturability due to the lowered melting point. These modifications highlight the potential for optimizing mechanical properties and processing efficiency in RHEAs through strategic compositional adjustments.

3.5. Strengthening mechanism

In RHEAs, the yield strength (σ_y) is typically attributed to solid solution strengthening ($\Delta\sigma_{ss}$), GB strengthening ($\Delta\sigma_{GB}$), and precipitation strengthening ($\Delta\sigma_P$). Due to the absence of precipitates in this RHEA, its σ_y can be expressed as [70]:

$$\sigma_y = \sigma_0 + \Delta\sigma_{ss} + \Delta\sigma_{GB} \quad (1)$$

σ_0 is the yield strength of the matrix, which can be estimated using the rule of mixtures:

$$\sigma_0 = \sum c_i \sigma_i \quad (2)$$

Here, c_i and σ_i are the concentration and yield strength of the i^{th} component, respectively, with the σ_i values available in Ref. [70]. The calculated σ_0 is 200–260 MPa.

The value of $\Delta\sigma_{ss}$ can be estimated using Eqs. (3–4) [70]:

$$\Delta\sigma_{ss} = \left(\sum \Delta\sigma_{ssi}^{3/2} \right)^{2/3} \quad (3)$$

$$\Delta\sigma_{ssi} = AGf_i^{4/3} c_i^{2/3} \quad (4)$$

where $\Delta\sigma_{ssi}$ is the solid solution strengthening contribution from the i^{th} constituent, $A = 0.085$ [71], representing a dimensionless material-specific constant, $G = 42.34$ GPa, denoting the shear modulus of the RHEA, and f_i is the misfit parameter of the i^{th} constituent. The value of f_i can be estimated using Eq. (5) [71]:

$$f_i = \xi(\delta G_i^2 + \beta^2 \delta r_i^2)^{1/2} \quad (5)$$

where $\xi = 2.5$ (for BCC alloy), $\beta = 3$, $\delta G_i'$ = corrected shear modulus misfit, and δr_i = atomic radius misfit [71]. Table 4 lists the calculated

Table 4

The atomic radius misfit (δr_i) and corrected shear modulus misfit ($\delta G_i'$) of each element in the Ti40Zr25Nb25Ta5Al5 RHEA.

Property	Ti	Zr	Nb	Ta	Al
δr_i (pm)	-6	12.6	-3.4	-3.2	-3.2
$\delta G_i'$	0.0990	-0.1587	-0.0689	0.5310	-0.2960

values of δr_i and $\delta G_i'$ for this RHEA. Combining the above contributions yields $\Delta\sigma_{ss} = 731.82$ MPa.

Finally, the value of $\Delta\sigma_{GB}$ can be estimated using the Hall-Petch relationship [72]:

$$\Delta\sigma_{GB} = Kd^{-1/2} \quad (6)$$

where $K = 430$ MPa $\mu\text{m}^{-1/2}$ [73] and $d = 131$ μm (the average grain size). This estimation leads to $\Delta\sigma_{GB} = 37.57$ MPa.

The combined solid solution strengthening and GB strengthening result in $\sigma_y = 970$ –1030 MPa, which aligns well with the yield strength of this alloy (960 MPa). This clarifies the primary strengthening mechanism of the Ti40Zr25Nb25Ta5Al5 RHEA.

3.6. Surface oxide film and electrochemical assessment

XPS spectra of Ti 2p, Nb 3d, Zr 3d, Ta 4 f and Al 2p peaks obtained from the as-cast RHEA surface are shown in Fig. 9a-d at a take-off angle of 0°. TiO_2 , ZrO_2 , Nb_2O_5 and Ta_2O_5 were detected as major oxides while a trace of Nb^{4+} and Al^{3+} was also detected from the spectra. It should be noted that the Al 2p peaks were superimposed on the Ta 5 s and Ti 3s plasmon. Such surface oxides form a continuous layer on the surface and have been investigated before [38,74–77]. These surface oxides influence the corrosion resistance of this RHEA [10,11,74,78,79].

Fig. 10 shows the potentiodynamic polarization curves of the as-cast Ti40Zr25Nb25Ta5Al5 RHEA compared with Ti-6Al-4V in Hank's solution at 37 °C. Table 5 summarises the fitted electrochemical properties. Corrosion potential (E_{corr}) and corrosion current density (i_{corr}) are estimated via the Tafel extrapolation [80–82]. The i_{corr} of as-cast RHEA is one order of magnitude lower than that of the Ti-6Al-4V alloy, while E_{corr} values are comparable. It indicates substantially higher corrosion resistance than Ti-6Al-4V. Additionally, the passivation current density (i_{pass}), for the as-cast Al-doped RHEA is also one order of magnitude lower than that of the Ti-6Al-4V alloy. This suggests that the surface of the as-cast RHEA is more readily passivated compared to Ti-6Al-4V, thereby offering more timely protection. XPS analyses revealed that

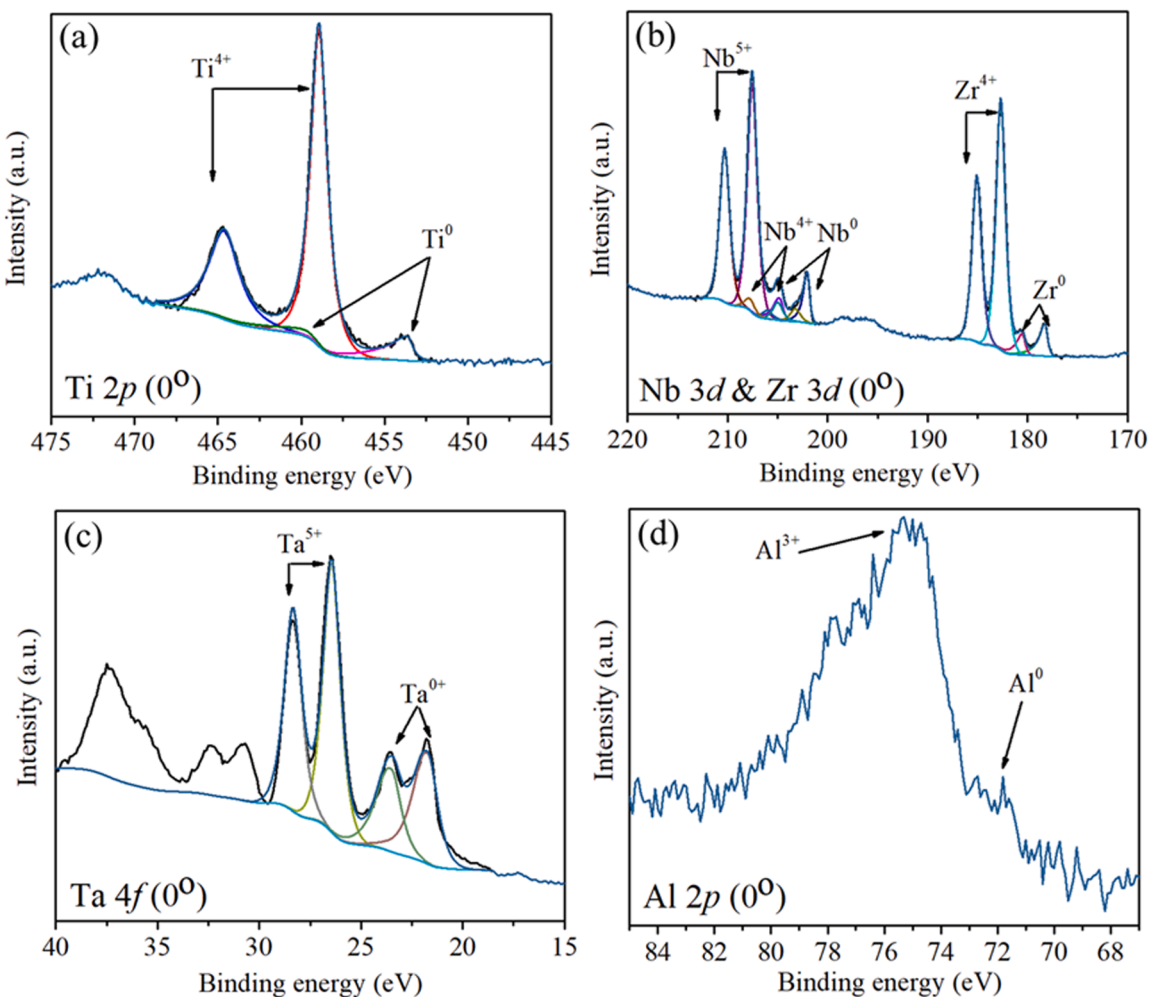


Fig. 9. XPS spectra of (a) Ti 2p, (b) Nb 3d & Zr 3d, (c) Ta 4f and (d) Al 2p peaks obtained from the as-cast Ti40Zr25Nb25Ta5Al5 RHEA measured at a take-off angle of 0° .

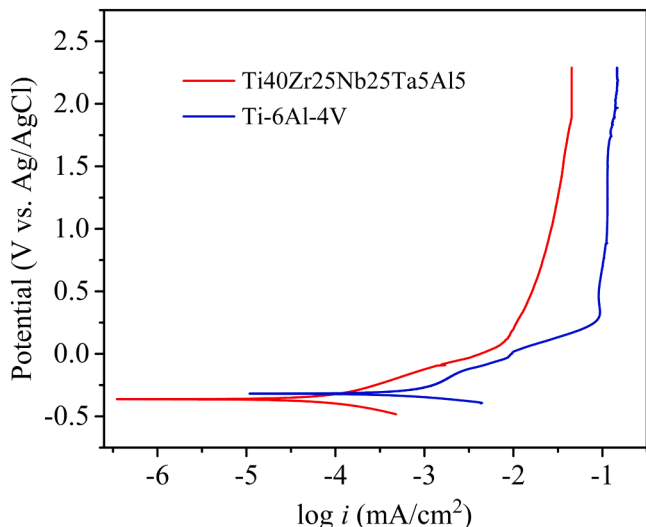


Fig. 10. Potentiodynamic polarization curves of the copper mould-cast Ti40Zr25Nb25Ta5Al5 RHEA and Ti-6Al-4V alloy in Hank's solution at 37°C .

the surface oxide film of the RHEA consists of TiO_2 , ZrO_2 , Nb_2O_5 , and Ta_2O_5 , with trace amounts of Nb^{4+} and Al^{3+} also detected. Consequently, the superior corrosion resistance can be attributed to the

Table 5

Electrochemical assessment of the as-cast Ti40Zr25Nb25Ta5Al5 RHEA and Ti-6Al-4V in Hank's solution at 37°C .

Material	E_{corr} (mV Ag/AgCl)	i_{corr} (mA/cm 2)	i_{pass} (mA/cm 2)
Ti-6Al-4V	-312.10 ± 9	7.51×10^{-4} $\pm 3 \times 10^{-4}$	9.12×10^{-2} $\pm 2.80 \times 10^{-2}$
Ti40Zr25Nb25Ta5Al5	-361.2 ± 3	6.22×10^{-5} $\pm 2 \times 10^{-4}$	$7.41 \times 10^{-3} \pm 1.00$ $\times 10^{-3}$

co-existence of TiO_2 , ZrO_2 , Nb_2O_5 , and Ta_2O_5 in the oxide film, as each oxide component is not only biocompatible but also highly corrosion-resistant, particularly Ta_2O_5 [38,78]. In contrast, the surface oxide film of the α - β Ti-6Al-4V alloy is predominantly composed of TiO_2 [83], which showed inferior performance in Hank's solution at 37°C .

Another key difference is that the Ti40Zr25Nb25Ta5Al5 RHEA is a single-phase (BCC) material, while the lamellar α - β Ti-6Al-4V alloy consists of two phases: hexagonal close-packed α and BCC β , which results in a significant α - β interfacial area. Generally, a single phase is preferred for improved corrosion resistance. However, no experimental evidence has yet been reported linking the corrosion resistance of α - β Ti-6Al-4V to the extent of its α - β interfacial area. This presents an opportunity for future research.

4. Conclusions

The following conclusions can be drawn from this experimental study of the as-cast Ti40Zr25Nb25Ta5Al5 RHEA.

- A new non-equiautomic Ti40Zr25Nb25Ta5Al5 RHEA was designed by tuning the Ti40Zr25Nb25Ta10 RHEA through replacing 5 at.% Ta with 5 at.% Al. This modification reduces the alloy density from 7.2 to 6.5 g/cm³ (calculated using the 'rule of mixtures') and increases the yield strength from 875 to 960 MPa, while still allowing the RHEA to achieve a high tensile ductility of about 17 %.
- The tensile fracture surface of the as-cast Ti40Zr25Nb25Ta5Al5 RHEA shows fine and severely distorted dimples. In addition to multiple dislocation activities, the formation of primary and secondary shear bands within individual grains plays an important role in enhancing the strength and tensile ductility of this RHEA.
- Compared to the mill-annealed medical-grade Ti-6Al-4V alloy, the as-cast Ti40Zr25Nb25Ta5Al5 RHEA has higher yield strength (960 MPa), better tensile ductility (17 %), lower elastic modulus (85 GPa), higher admissible strain (1.12 %) and better corrosion resistance in Hank's solution. This new RHEA can be considered as a promising candidate alloy for biomedical applications.
- The addition of 5 at.% Al or 1.8 wt.% Al notably reduces the grain size and increases the yield strength of the as-cast Ti40Zr25Nb25-Ta5Al5 RHEA while allowing the as-cast RHEA to maintain a high tensile ductility (about 17 %). Thus, a small addition of Al proves to be a very effective way of modifying the Ti-Zr-Nb-Ta-based RHEAs.

CRediT authorship contribution statement

Mustafi Labani: Writing – review & editing, Writing – original draft, Visualization, Validation, Software, Methodology, Investigation, Formal analysis, Data curation, Conceptualization. **Nguyen V.T.:** Methodology, Conceptualization. **Song T.:** Writing – review & editing, Validation, Supervision, Methodology. **Chen X.-B.:** Writing – review & editing, Validation, Supervision, Methodology, Formal analysis. **Fabijanic D. M.:** Writing – review & editing, Visualization, Validation, Supervision, Methodology. **Qian M.:** Writing – review & editing, Visualization, Validation, Supervision, Resources, Project administration, Methodology, Investigation, Funding acquisition, Formal analysis, Data curation, Conceptualization.

Declaration of Competing Interest

The authors declare that they have no known competing financial interests or personal relationships that could have appeared to influence the work reported in this paper.

Acknowledgements

This work was funded by the Australian-India Strategic Research Fund under AISRF53731 (Advanced manufacturing of new high entropy alloys). The authors acknowledge the technical assistance of the RMIT Microscopy and Microanalysis Facility (RMMF). We express our gratitude to Dr. Billy Murdoch from the RMMF for his technical assistance during the XPS experiment. Our heartfelt thanks go to Dr. Qiushi Deng from the School of Engineering, RMIT University, Australia, for his support with the electrochemical corrosion experiment.

References

- [1] O. Senkov, G. Wilks, D. Miracle, C. Chuang, P. Liaw, Refractory high-entropy alloys, *Intermetallics* 18 (2010) 1758–1765, <https://doi.org/10.1016/j.intermet.2010.05.014>.
- [2] Y. Zou, S. Maiti, W. Steurer, R. Spolenak, Size-dependent plasticity in an Nb25Mo25Ta25W25 refractory high-entropy alloy, *Acta Mater.* 65 (2014) 85–97, <https://doi.org/10.1016/j.actamat.2013.11.049>.
- [3] Y. Zou, H. Ma, R. Spolenak, Ultrastrong ductile and stable high-entropy alloys at small scales, *Nat. Commun.* 6 (2015) 1–8, <https://doi.org/10.1038/ncomms8748>.
- [4] S.P. Wang, E. Ma, J. Xu, New ternary equi-atomic refractory medium-entropy alloys with tensile ductility: Hafnium versus titanium into NbTa-based solution, *Intermetallics* 107 (2019) 15–23, <https://doi.org/10.1016/j.intermet.2019.01.004>.
- [5] Z. Lei, X. Liu, Y. Wu, H. Wang, S. Jiang, S. Wang, X. Hui, Y. Wu, B. Gault, P. Kontis, Enhanced strength and ductility in a high-entropy alloy via ordered oxygen complexes, *Nature* 563 (2018) 546–550, <https://doi.org/10.1038/s41586-018-0685-y>.
- [6] D.B. Miracle, O.N. Senkov, A critical review of high entropy alloys and related concepts, *Acta Mater.* 122 (2017) 448–511, <https://doi.org/10.1016/j.actamat.2016.08.081>.
- [7] O.N. Senkov, S. Senkova, C. Woodward, D.B. Miracle, Low-density, refractory multi-principal element alloys of the Cr–Nb–Ti–V–Zr system: microstructure and phase analysis, *Acta Mater.* 61 (2013) 1545–1557, <https://doi.org/10.1016/j.actamat.2012.11.032>.
- [8] Y. Shi, B. Yang, P.K. Liaw, Corrosion-resistant high-entropy alloys: a review, *Metals* 7 (2017) 43, <https://doi.org/10.3390/met7020043>.
- [9] J. Li, X. Yang, R. Zhu, Y. Zhang, Corrosion and serration behaviors of TiZr0.5NbCr0.5V Mo high entropy alloys in aqueous environments, *Metals* 4 (2014) 597–608, <https://doi.org/10.3390/met4040597>.
- [10] L. Mustafi, V.T. Nguyen, T. Song, Q. Deng, B.J. Murdoch, X.B. Chen, D. M. Fabijanic, M. Qian, A strong and ductile biocompatible Ti40Zr25Nb25Ta5Mo5 high entropy alloy, *J. Mater. Res. Technol.* 30 (2024) 7885–7895, <https://doi.org/10.1016/j.jmrt.2024.05.118>.
- [11] L. Mustafi, V.T. Nguyen, T. Song, Q. Deng, L. Jiang, X.B. Chen, D.M. Fabijanic, M. Qian, Effect of oxygen on the microstructure, tensile properties and deformation behaviours of a biocompatible Ti40Zr25Nb25Ta10 high entropy alloy, *J. Mater. Sci. Technol.* 214 (2025) 62–73, <https://doi.org/10.1016/j.jmst.2024.06.022>.
- [12] J.R. Sin, Investigation of hafnium for biomedical applications: corrosion and tribocorrosion in simulated body fluids, *Luleå tekniska universitet* (2013).
- [13] M. Yan, M. Qian, C. Kong, M.S. Dargusch, Impacts of trace carbon on the microstructure of as-sintered biomedical Ti-15Mo alloy and reassessment of the maximum carbon limit, *Acta Biomater.* 10 (2014) 1014–1023, <https://doi.org/10.1016/j.actbio.2013.10.034>.
- [14] K. Moghadasi, M.S. Mohd Isa, M.A. Ariffin, M.Z. Mohd jamil, S. Raja, B. Wu, M. Yamani, M.R. Bin Muhamad, F. Yusof, M.F. Jamaludin, M.Sb Ab Karim, Bb Abdul Razak, Nb Yusoff, A review on biomedical implant materials and the effect of friction stir based techniques on their mechanical and tribological properties, *J. Mater. Res. Technol.* 17 (2022) 1054–1121, <https://doi.org/10.1016/j.jmrt.2022.01.050>.
- [15] Y. Okazaki, Y. Ito, A. Ito, T. Tateishi, Effect of alloying elements on mechanical properties of titanium alloys for medical implants, *Mater. Trans. JIM* 34 (1993) 1217–1222, <https://doi.org/10.2320/matertrans1989.34.1217>.
- [16] Y. Okazaki, S. Rao, T. Tateishi, Y. Ito, Cytocompatibility of various metal and development of new titanium alloys for medical implants, *Mater. Sci. Eng.: A* 243 (1998) 250–256, [https://doi.org/10.1016/S0921-5093\(97\)00809-5](https://doi.org/10.1016/S0921-5093(97)00809-5).
- [17] O. Senkov, C. Woodward, D. Miracle, Microstructure and properties of aluminum-containing refractory high-entropy alloys, *Jom* 66 (2014) 2030–2042, <https://doi.org/10.1007/s11837-014-1066-0>.
- [18] O. Senkov, S. Senkova, C. Woodward, Effect of aluminum on the microstructure and properties of two refractory high-entropy alloys, *Acta Mater.* 68 (2014) 214–228, <https://doi.org/10.1016/j.actamat.2014.01.029>.
- [19] C.-M. Lin, C.-C. Juan, C.-H. Chang, C.-W. Tsai, J.-W. Yeh, Effect of Al addition on mechanical properties and microstructure of refractory AlxHfNbTaTiZr alloys, *J. Alloy. Compd.* 624 (2015) 100–107, <https://doi.org/10.1016/j.jallcom.2014.11.064>.
- [20] N.A. Ley, S. Segovia, S. Gorrissen, M.L. Young, Characterization and modeling of NbNiTaTiW and NbNiTaTiW-Al refractory high-entropy alloys, *Metall. Mater. Trans. A* 50 (2019) 4867–4876, <https://doi.org/10.1007/s11661-019-05384-w>.
- [21] O. Senkov, J. Jensen, A. Pilchak, D. Miracle, H. Fraser, Compositional variation effects on the microstructure and properties of a refractory high-entropy superalloy AlMo0.5NbTa0.5TiZr, *Mater. Des.* 139 (2018) 498–511, <https://doi.org/10.1016/j.matdes.2017.11.033>.
- [22] P.S. Ocaño, S.G. Fries, I. Lopez-Galilea, R.D. Kamachali, J. Roik, L.A. Jácome, The AlMo0.5NbTa0.5TiZr refractory high entropy superalloy: experimental findings and comparison with calculations using the CALPHAD method, *Mater. Des.* 217 (2022) 110593, <https://doi.org/10.1016/j.matdes.2022.110593>.
- [23] B. O'Brien, M. Bruzzi, 1.104 - Shape Memory Alloys for Use in Medicine, in: P. Ducheyne (Ed.), *Comprehensive Biomaterials*, Elsevier, Oxford, 2011, pp. 49–72.
- [24] V. Nguyen, M. Qian, Z. Shi, T. Song, L. Huang, J. Zou, Compositional design of strong and ductile (tensile) Ti-Zr-Nb-Ta medium entropy alloys (MEAs) using the atomic mismatch approach, *Mater. Sci. Eng.: A* 742 (2019) 762–772, <https://doi.org/10.1016/j.msea.2018.11.054>.
- [25] V.T. Nguyen, M. Qian, Z. Shi, T. Song, L. Huang, J. Zou, A novel quaternary equiatomic Ti-Zr-Nb-Ta medium entropy alloy (MEA), *Intermetallics* 101 (2018) 39–43, <https://doi.org/10.1016/j.intermet.2018.07.008>.
- [26] K.L. Wapner, Implications of metallic corrosion in total knee arthroplasty, *Clin. Orthop. Relat. Res.* 271 (1991) 12–20.
- [27] Y. Zhang, Y.J. Zhou, J.P. Lin, G.L. Chen, P.K. Liaw, Solid-solution phase formation rules for multi-component alloys, *Adv. Eng. Mater.* 10 (2008) 534–538, <https://doi.org/10.1002/adem.200700240>.

- [28] G. Sheng, C.T. Liu, Phase stability in high entropy alloys: formation of solid-solution phase or amorphous phase, *Prog. Nat. Sci.: Mater. Int.* 21 (2011) 433–446, [https://doi.org/10.1016/S1002-0071\(12\)60080-X](https://doi.org/10.1016/S1002-0071(12)60080-X).
- [29] S. Guo, Phase selection rules for cast high entropy alloys: an overview, *Mater. Sci. Technol.* 31 (2015) 1223–1230, <https://doi.org/10.1179/1743284715Y.0000000018>.
- [30] N.D. Stepanov, D.G. Shaysultanov, G.A. Salishchev, M.A. Tikhonovsky, Structure and mechanical properties of a light-weight AlNbTiV high entropy alloy, *Mater. Lett.* 142 (2015) 153–155, <https://doi.org/10.1016/j.matlet.2014.11.162>.
- [31] O.A. Waseem, H.J. Ryu, Powder metallurgy processing of a WxTaTiVCr high-entropy alloy and its derivative alloys for fusion material applications, *Sci. Rep.* 7 (2017) 1926, <https://doi.org/10.1038/s41598-017-02168-3>.
- [32] D. Abou-Ras, R. Caballero, C. Fischer, C. Kaufmann, I. Lauermann, R. Mainz, H. Monig, A. Schopke, C. Stephan, C. Streeck, Comprehensive comparison of various techniques for the analysis of elemental distributions in thin films, *Microsc. Microanal.* 17 (2011) 728–751, <https://doi.org/10.1017/S1431927611000523>.
- [33] S.E. Harandi, P.C. Banerjee, C.D. Easton, R.K. Singh Raman, Influence of bovine serum albumin in Hanks' solution on the corrosion and stress corrosion cracking of a magnesium alloy, *Mater. Sci. Eng.: C* 80 (2017) 335–345, <https://doi.org/10.1016/j.msec.2017.06.002>.
- [34] A. Bal-Price, S. Coecke, Guidance on Good Cell Culture Practice (GCCP), in: M. Aschner, C. Suñol, A. Bal-Price (Eds.), *Cell Culture Techniques, Neuromethods*, in, Humana Press, Totowa, NJ, USA, 2011, <https://doi.org/10.1007/978-1-61779-077-5>.
- [35] R.I. Freshney, *Culture of animal cells: a manual of basic technique and specialized applications*, John Wiley & Sons, 2015.
- [36] C.D. Helgason, C.L. Miller, *Basic cell culture protocols*, Humana Press, Totowa, NJ, 2005.
- [37] A.R. Denton, N.W. Ashcroft, Vegard's law, *Phys. Rev. A* 43 (6) (1991) 3161, <https://doi.org/10.1103/PhysRevA.43.3161>.
- [38] L. Mustafi, V.T. Nguyen, S.L. Lu, T. Song, B.J. Murdoch, D.M. Fabijanic, M. Qian, Microstructure, tensile properties and deformation behaviour of a promising biocompatible new Ti35Zr15Nb25Ta25 medium entropy alloy (MEA), *Mater. Sci. Eng.: A* 824 (2021) 141805, <https://doi.org/10.1016/j.msea.2021.141805>.
- [39] M. Rappaz, A. Jacot, W.J. Boettinger, Last-stage solidification of alloys: theoretical model of dendrite-arm and grain coalescence, *Metall. Mater. Trans. A* 34 (2003) 467–479, <https://doi.org/10.1007/s11661-003-0083-3>.
- [40] H. Liu, S. Lu, Y. Zhang, H. Chen, Y. Chen, M. Qian, Migration of solidification grain boundaries and prediction, *Nat. Commun.* 13 (2022) 5910, <https://doi.org/10.1038/s41467-022-33482-8>.
- [41] A. Takeuchi, A. Inoue, Classification of bulk metallic glasses by atomic size difference, heat of mixing and period of constituent elements and its application to characterization of the main alloying element, *Mater. Trans.* 46 (12) (2005) 2817–2829, <https://doi.org/10.2320/matertrans.46.2817>.
- [42] X. Zhang, W. Wang, J. Wu, S. Wang, J. Sun, J.Y. Chung, S.J. Pennycook, Deformation twinning in Ti48. 9Zr32. 6Nb12. 6Ta6. 5 medium entropy alloy, *Mater. Sci. Eng.: A* 809 (2021) 140931, <https://doi.org/10.1016/j.msea.2021.140931>.
- [43] J. Zýka, J. Málek, J. Veselý, F. Lukáč, J. Čížek, J. Kuríplach, O. Melikhova, Microstructure and room temperature mechanical properties of different 3 and 4 element medium entropy alloys from HfNbTaTiZr system, *Entropy* 21 (2019) 114, <https://doi.org/10.3390/e21020114>.
- [44] J. Liu, X. Zhang, Z. Yuan, Structures and properties of biocompatible Ti-Zr-Nb-Fe-Mo medium entropy alloys, *Mater. Today Commun.* 32 (2022) 103808, <https://doi.org/10.1016/j.mtcomm.2022.103808>.
- [45] T. Aoki, I. Okafor, I. Watanabe, M. Hattori, Y. Oda, T. Okabe, Mechanical properties of cast Ti-6Al-4V-XCu alloys, *J. Oral. Rehabil.* 31 (2004) 1109–1114, <https://doi.org/10.1111/j.1365-2842.2004.01347.x>.
- [46] K. Wang, The use of titanium for medical applications in the USA, *Mater. Sci. Eng.: A* 213 (1996) 134–137, [https://doi.org/10.1016/0921-5093\(96\)10243-4](https://doi.org/10.1016/0921-5093(96)10243-4).
- [47] Y. Li, C. Yang, H. Zhao, S. Qu, X. Li, Y. Li, New developments of Ti-based alloys for biomedical applications, *Materials* 7 (2014) 1709–1800, <https://doi.org/10.3390/ma7031709>.
- [48] S. Ozan, J. Lin, Y. Li, R. Ipek, C. Wen, Development of Ti–Nb–Zr alloys with high elastic admissible strain for temporary orthopedic devices, *Acta Biomater.* 20 (2015) 176–187, <https://doi.org/10.1016/j.actbio.2015.03.023>.
- [49] D. Kuroda, M. Niinomi, M. Morinaga, Y. Kato, T. Yashiro, Design and mechanical properties of new β type titanium alloys for implant materials, *Mater. Sci. Eng.: A* 243 (1998) 244–249, [https://doi.org/10.1016/S0921-5093\(97\)00080-3](https://doi.org/10.1016/S0921-5093(97)00080-3).
- [50] K.K. Wang, L.J. Gustavson, J.H. Dumbleton, Microstructure and properties of a new beta titanium alloy, Ti-12Mo-6Zr-2Fe, developed for surgical implants. *Medical Applications of Titanium and Its Alloys: The Material and Biological Issues*, ASTM International, 1996.
- [51] F. ASTM, Standard Specification for Wrought Titanium-6Aluminum-4Vanadium ELI (Extra Low Interstitial) Alloy for Surgical Implant Applications (UNS R56401), *ASTM F136-13* (2013).
- [52] W. Xu, S. Sun, J. Elambasseri, Q. Liu, M. Brandt, M. Qian, Ti-6Al-4V additively manufactured by selective laser melting with superior mechanical properties, *Jom* 67 (2015) 668–673, <https://doi.org/10.1007/s11837-015-1297-8>.
- [53] H.E. Boyer, ASM International, second ed., Materials Park, OH, 2002.
- [54] M. Niinomi, Mechanical properties of biomedical titanium alloys, *Mater. Sci. Eng.: A* 243 (1998) 231–236, [https://doi.org/10.1016/S0921-5093\(97\)00086-X](https://doi.org/10.1016/S0921-5093(97)00086-X).
- [55] C.-W. Lin, C.-P. Ju, J.-H.C. Lin, Comparison among mechanical properties of investment-cast cp Ti, Ti-6Al-7Nb and Ti-15Mo-1Bi alloys, *Mater. Trans.* 45 (2004) 3028–3032, <https://doi.org/10.2320/matertrans.45.3028>.
- [56] Y. Kajima, H. Doi, A. Takaichi, T. Hanawa, N. Wakabayashi, Surface characteristics and castability of Zr-14Nb alloy dental castings, *Dent. Mater.* 33 (2014) 631–637, <https://doi.org/10.4012/dmj.2014-117>.
- [57] I. Polmear, D. St.John, J.-F. Nie, M. Qian, 7 - Titanium Alloys, in: I. Polmear, D. St.John, J.-F. Nie, M. Qian (Eds.), *Light Alloys (Fifth Edition)*, Butterworth-Heinemann, Boston, 2017, pp. 369–460.
- [58] X. Wang, S. Xu, S. Zhou, W. Xu, M. Leary, P. Choong, M. Qian, M. Brandt, Y.M. Xie, Topological design and additive manufacturing of porous metals for bone scaffolds and orthopaedic implants: a review, *Biomaterials* 83 (2016) 127–141, <https://doi.org/10.1016/j.biomaterials.2016.01.012>.
- [59] X. Tong, Q. Sun, D. Zhang, K. Wang, Y. Dai, Z. Shi, Y. Li, M. Dargusch, S. Huang, J. Ma, Impact of scandium on mechanical properties, corrosion behavior, friction and wear performance, and cytotoxicity of a β -type Ti-24Nb-38Zr-2Mo alloy for orthopedic applications, *Acta Biomater.* 134 (2021) 791–803, <https://doi.org/10.1016/j.actbio.2021.07.061>.
- [60] S. Ozan, J. Lin, W. Wang, Y. Zhang, Y. Li, C. Wen, Effect of thermomechanical treatment on the mechanical and microstructural evolution of a β -type Ti-40.7Zr-24.8Nb alloy, *Bioact. Mater.* 4 (2019) 303–311, <https://doi.org/10.1016/j.bioactmat.2019.10.007>.
- [61] Y. Song, D. Xu, R. Yang, D. Li, W. Wu, Z. Guo, Theoretical study of the effects of alloying elements on the strength and modulus of β -type bio-titanium alloys, *Mater. Sci. Eng.: A* 260 (1999) 269–274, [https://doi.org/10.1016/S0921-5093\(98\)00886-7](https://doi.org/10.1016/S0921-5093(98)00886-7).
- [62] Z. Li, W. Lai, X. Tong, D. You, W. Li, X. Wang, Design of TiZrNbTa multi-principal element alloys with outstanding mechanical properties and wear resistance, *Mater. Sci. Eng.: A* 845 (2022) 143203, <https://doi.org/10.1016/j.msea.2022.143203>.
- [63] H. Zhong, T. Song, R. Das, C. Li, J. Gu, M. Qian, Ultralight, ductile metal mechanical metamaterials with super elastic admissible strain (0.1), *J. Mater. Sci. Technol.* 162 (2023) 227–233, <https://doi.org/10.1016/j.jmst.2023.03.043>.
- [64] J. Zhang, S. Hao, D. Jiang, Y. Huan, L. Cui, Y. Liu, Y. Ren, H. Yang, Dual phase synergy enabled large elastic strains of nano inclusions in a dislocation slip matrix composite, *Nano Lett.* 18 (2018) 2976–2983, <https://doi.org/10.1021/acs.nanolett.8b00427>.
- [65] G. Dirras, H. Couque, L. Lilenstein, A. Heczel, D. Tingaud, J.-P. Couzinié, L. Perrière, J. Gubicza, I. Guillot, Mechanical behavior and microstructure of Ti20Hf20Zr20Ta20Nb20 high-entropy alloy loaded under quasi-static and dynamic compression conditions, *Mater. Charact.* 111 (2016) 106–113, <https://doi.org/10.1016/j.matchar.2015.11.018>.
- [66] T. Furuta, S. Kuramoto, J. Hwang, K. Nishino, T. Saito, Elastic deformation behavior of multi-functional Ti–Nb–Ta–Zr–O alloys, *Mater. Trans.* 46 (2005) 3001–3007, <https://doi.org/10.2320/matertrans.46.3001>.
- [67] S. Wang, M. Wu, D. Shu, B. Sun, Kinking in a refractory TiZrHfNbO₇ medium-entropy alloy, *Mater. Lett.* 264 (2020) 127369, <https://doi.org/10.1016/j.mattlet.2020.127369>.
- [68] Y. Bu, Y. Wu, Z. Lei, X. Yuan, H. Wu, X. Feng, J. Liu, J. Ding, Y. Lu, H. Wang, Z. Lu, W. Yang, Local chemical fluctuation mediated ductility in body-centered-cubic high-entropy alloys, *Mater. Today* 46 (2021) 28–34, <https://doi.org/10.1016/j.mattod.2021.02.022>.
- [69] J. Pang, H. Zhang, Z. Zhu, H. Fu, H. Li, A. Wang, Z. Li, H. Zhang, Ductile Ti1. 5ZrNbAl0. 3 refractory high entropy alloy with high specific strength, *Mater. Lett.* 290 (2021) 129428, <https://doi.org/10.1016/j.mattlet.2021.129428>.
- [70] J. Gong, Y. Li, W. Wu, Y. Wang, Z. Chen, Chemical ordering enhancing mechanical properties of Nb2Ti35V5Zr35Alx refractory high-entropy alloys, *J. Alloy. Compd.* 1017 (2025) 178990, <https://doi.org/10.1016/j.jallcom.2025.178990>.
- [71] Y. Liu, B. Yu, Y. Chen, H. Chen, Y. Li, Z. Cai, G. Xie, Effect of oxygen on microstructure and mechanical properties of (TiZrNbTa) 100-xOx (x = 0~ 6.0) high-entropy alloys, *Mater. Sci. Eng.: A* 924 (2025) 147800, <https://doi.org/10.1016/j.msea.2025.147800>.
- [72] N.J. Petch, The cleavage strength of polycrystals, *J. Iron Steel Inst.* 174 (1953) 25–28.
- [73] Z.C. Cordero, B.E. Knight, C.A. Schuh, Six decades of the Hall–Petch effect—a survey of grain-size strengthening studies on pure metals, *Int. Mater. Rev.* 61 (2016) 495–512, <https://doi.org/10.1080/09506608.2016.1191808>.
- [74] N. Hua, W. Wang, Q. Wang, Y. Ye, S. Lin, L. Zhang, Q. Guo, J. Brechtl, P.K. Liaw, Mechanical, corrosion, and wear properties of biomedical Ti–Zr–Nb–Ta–Mo high entropy alloys, *J. Alloy. Compd.* 861 (2021) 157997, <https://doi.org/10.1016/j.jallcom.2020.157997>.
- [75] A. Motallebzadeh, N.S. Peighambardoust, S. Sheikh, H. Murakami, S. Guo, D. Canadinc, Microstructural, mechanical and electrochemical characterization of TiZrTaHfNb and Ti1. 5ZrTa0. 5Hf0. 5Nb0. 5 refractory high-entropy alloys for biomedical applications, *Intermetallics* 113 (2019) 106572, <https://doi.org/10.1016/j.intermet.2019.106572>.
- [76] I. Milošev, G. Žerjav, J.M. Calderon Moreno, M. Popa, Electrochemical properties, chemical composition and thickness of passive film formed on novel Ti–20Nb–10Zr–5Ta alloy, *Electrochim. Acta* 99 (2013) 176–189, <https://doi.org/10.1016/j.electacta.2013.03.086>.
- [77] C. Vasilescu, S. Drob, J.C. Moreno, P. Osiceanu, M. Popa, E. Vasilescu, M. Marcu, P. Drob, Long-term corrosion resistance of new Ti–Ta–Zr alloy in simulated physiological fluids by electrochemical and surface analysis methods, *Corros. Sci.* 93 (2015) 310–323, <https://doi.org/10.1016/j.corsci.2015.01.038>.
- [78] S. Mendis, W. Xu, H. Tang, L. Jones, D. Liang, R. Thompson, P. Choong, M. Brandt, M. Qian, Characteristics of oxide films on Ti-(10–75) Ta alloys and their corrosion performance in an aerated Hank's balanced salt solution, *Appl. Surf. Sci.* 506 (2020) 145013, <https://doi.org/10.1016/j.apsusc.2019.145013>.
- [79] Y.-f Xu, Y.-f Xiao, D.-q Yi, H.-q Liu, L. Wu, J. Wen, Corrosion behavior of Ti–Nb–Ta–Zr–Fe alloy for biomedical applications in Ringer's solution, *Trans. Nonferrous Met.* 33 (2023) 113–118, <https://doi.org/10.1016/j.tnfm.2023.01.011>.

- Met. Soc. China 25 (2015) 2556–2563, [https://doi.org/10.1016/S1003-6326\(15\)63875-4](https://doi.org/10.1016/S1003-6326(15)63875-4).
- [80] E. McCafferty, Validation of corrosion rates measured by the Tafel extrapolation method, *Corros. Sci.* 47 (2005) 3202–3215, <https://doi.org/10.1016/j.corsci.2005.05.046>.
- [81] M.A. Amin, K. Khaled, S.A. Fadl-Allah, Testing validity of the Tafel extrapolation method for monitoring corrosion of cold rolled steel in HCl solutions—experimental and theoretical studies, *Corros. Sci.* 52 (2010) 140–151, <https://doi.org/10.1016/j.corsci.2009.08.055>.
- [82] E. Poorqasemi, O. Abootalebi, M. Peikari, F. Haqdar, Investigating accuracy of the Tafel extrapolation method in HCl solutions, *Corros. Sci.* 51 (2009) 1043–1054, <https://doi.org/10.1016/j.corsci.2009.03.001>.
- [83] A. Biswas, P.V.S. Srikant, I. Manna, U.K. Chatterjee, J.D. Majumdar, Chemical oxidation of Ti-6Al-4V for improved wear and corrosion resistance, *Surf. Eng.* 24 (2008) 442–446, <https://doi.org/10.1179/174329408x286097>.